Cryo-EM and Molecular Dynamics Simulations Reveal Hidden Conformational Dynamics Controlling Ammonia Transport in Human Asparagine Synthetase

Adriana Coricello[1,9], Wen Zhu[2,*], Antonio Lupia[3,10], Carmen Gratteri[1], Matthijn Vos[4], Vincent Chaptal[5], Stefano Alcaro[1,4,*], Yuichiro Takagi[6,*] & Nigel G. J. Richards[7,8,*]

[1]Dipartimento di Scienze della Salute, Università "Magna Græcia" di Catanzaro, 88100 Catanzaro, Italy

[2]Department of Chemistry & Biochemistry, Florida State University, Tallahassee, FL 32306, USA

[3]Net4Science Academic Spin-Off, Università "Magna Græcia" di Catanzaro, 88100 Catanzaro, Italy

[4]NanoImaging Core Facility, Centre de Resources et Recherches Technologiques, Institut Pasteur, 75015 Paris, France

[5]Molecular Microbiology and Structural Biochemistry Laboratory, CNRS UMR 5086, University of Lyon, 69367 Lyon, France

[6]Department of Biochemistry & Molecular Biology, Indiana University School of Medicine, Indianapolis, IN 46202, USA

[7]School of Chemistry, Cardiff University, Park Place, Cardiff CF10 3AT, UK

[8]Foundation for Applied Molecular Evolution, Alachua, FL 32615, USA

[9]Present address: Dipartimento di Scienze Biomolecolari, Università degli Studi di Urbino "Carlo Bo", 61029 Urbino, Italy

[10]Present address: Dipartimento di Scienze della vita e dell'ambiente, Università degli Studi di Cagliari, 09042 Cagliari, Italy

[*]Co-corresponding author

ABSTRACT

How dynamical motions in enzymes might be linked to catalytic function is of significant general interest, although almost all relevant experimental data, to date, has been obtained for enzymes with a single active site. Recent advances in X-ray crystallography and cryogenic electron microscopy offer the promise of elucidating dynamical motions for proteins that are not amenable to study using solution-phase NMR methods. Here we use 3D variability analysis (3DVA) of an EM structure for human asparagine synthetase (ASNS) in combination with atomistic molecular dynamics (MD) simulations to detail how dynamic motions of a single side chain mediates interconversion of the open and closed forms of a catalytically relevant intramolecular tunnel, thereby regulating catalytic function. Our 3DVA results are consistent with those obtained independently from MD simulations, which further suggest that formation of a key reaction intermediate acts to stabilize the open form of the tunnel in ASNS to permit ammonia translocation and asparagine formation. This conformational selection mechanism for regulating ammonia transfer in human ASNS contrasts sharply with those employed in other glutamine-dependent amidotransferases that possess a homologous glutaminase domain. Our work illustrates the power of cryo-EM to identify localized conformational changes and hence dissect the conformational landscape of large proteins. When combined with MD simulations, 3DVA is a powerful approach to understanding how conformational dynamics regulate function in metabolic enzymes with multiple active sites.

There is considerable general interest in understanding how dynamical motions in enzymes might be linked to function[1-5], although their precise contribution to catalysis remains the subject of debate[6,7]. Certainly, allosteric regulation of enzyme activity depends on residue motions[8,9], and computer-based simulations[10,11] support the idea that altered dynamical motions can be correlated with improvements in the catalytic efficiency of "designer" enzymes as they undergo optimization by directed evolution[12,13]. Moreover, experimental evidence has been published that supports the existence of thermal networks in enzymes, which mediate energy transfer between the active site and external solvent[14,15]. Dynamical motions have also been shown to mediate rapid interconversion of thermally accessible conformational states in enzymes, although many of these states are not catalytically competent[16]. It is therefore thought that substrate binding biases the conformational ensemble of the free enzyme to structures in which reaction can take place[17,18]. These ideas have been mostly developed, however, from NMR studies on enzymes that mostly possess only a single active site. Much less is known about how dynamical motions impact catalysis in enzymes that possess two, or more, active sites, such as the glutamine-dependent amidotransferases[19-21] or tryptophan synthase[22]. In general, these enzymes are too large for routine NMR-based studies of their dynamical motions in solution[23].

The past decade has seen rapid advances in new experimental techniques for observing the structural dynamics of proteins[3,24-26]. In particular, methods to analyze EM-derived maps[27] are providing new capabilities to obtain information on the dynamical motions of enzymes directly from the data[28,29]. How these motions are affected by external conditions, including buffer pH and concentration, ligand binding and temperature[30], can now (in principle) be examined. We now report the application of this strategy to understand the conformational dynamics of human ASNS, a Class II glutamine-dependent amidotransferase that mediates asparagine biosynthesis[31,32]. ASNS is of considerable biomedical interest, having been linked to metastatic progression in breast cancer[33], sarcoma cell proliferation[34], and decreased effectiveness of clinical treatments for acute lymphoblastic leukemia[35]. ASNS variants are also

strongly correlated with impaired neural development in children[36], pointing to the importance of gaining an in-depth understanding of catalytic mechanism and regulation of the enzyme. Structural[37,38] and biochemical studies show that ASNS is built from two domains, each of which contains an active site that catalyzes one of the "half-reactions" needed for the overall conversion of aspartate to asparagine (Supplementary Fig. S1)[39-41]. As in all other glutamine-dependent enzymes, catalytic turnover requires that ammonia must be transported between the two active sites through the intramolecular tunnel[42,43]. In this work, we have been able to establish the role of a single residue, Arg-142, in mediating the interconversion of the open and closed forms of this tunnel using both cryo-EM[44], and atomistic MD simulations[45,46]. Our analysis also provides the first molecular understanding of how ligand binding in the synthetase active site facilitates catalytic turnover by stabilizing the open form of the tunnel. This mechanism of regulating ammonia transfer in ASNS sharply differs from those operating in other Class II glutamine-dependent amidotransferases[47,48]. Finally, because we observe interconversion of the open and closed forms of the tunnel in MD trajectories of the free enzyme, our results support the hypothesis that conformational selection is playing a role in catalytic turnover for an enzyme with two active sites[17,18].

RESULTS

Structure determination of human ASNS by cryo-EM.

Human ASNS was expressed in insect cells and purified as described previously[49,50], except that purification was performed under reducing conditions to preserve a native state of the enzyme (see Methods). Single-particle images of unmodified, recombinant human ASNS (apo-ASNS) were collected and processed using cryoSPARC v3.2.2.[51] To test the native state of ASNS in an unbiased fashion, the "blob particle picker" option of cryoSPARC was used to select ~1.2 million particles followed by several rounds of 2D classification as well as *ab initio* reconstructions, giving a final total of 12 initial reconstructions (Supplementary Fig. S2). Eleven of these reconstructions exhibited small densities (Supplementary Fig. S2d), which

were further processed because they might correspond to a monomeric form of the enzyme (Supplementary Fig. S2f). We have not been able to converge these into a high-resolution map corresponding to the ASNS monomer (Supplementary Fig. S2f). The twelfth reconstruction clearly resembled the "head-to-head" ASNS dimer seen in the X-ray crystal structure (Supplementary Figs. S2d and S3)[37]. No initial 3D reconstruction resembling the "head-to-tail" dimer (Supplementary Fig. S6) seen in the X-ray structure of the bacterial homolog (AS-B)[38] was found. Realizing that the EM map of ASNS was similar to the crystal structure (Supplementary Fig. S6), we used a template-based particle picking strategy to pick good particles efficiently. Data processing (see Methods) eventually gave rise to a map with 3.5 Å overall resolution (Supplementary Figs. S3-S5, Table S1). The model derived from EM map was generated by utilizing our previous crystal structure of DON-modified human ASNS (PDB: 6GQ3)[37] (Fig. 1).

Our new EM structure confirms many of the conclusions reached on the basis of the high-resolution X-ray crystal structure of human ASNS[37] in which the Cys-1 side chain is modified by treatment with 6-diazo-5-oxo-L-norleucine (DON)[52]. First, it clearly shows that two monomers of unmodified human ASNS in the native state form a "head-to-head" dimer as a result of intermolecular interactions involving residues 31-34 in the adjacent N-terminal domains. The antiparallel orientation of these two segments places the side chains of Arg-32 and Glu-34 (monomer A) so that they can form salt bridges with Glu-34 and Arg-32 (monomer B), respectively (Fig. 1d). Moreover, Phe-31 and Phe-33 in both monomers form a hydrophobic cluster on the other face of the dimerization motif that likely contributes to the stability of the dimer interface in water (Fig. 1d). These contacts between the N-terminal domains of the ASNS monomers are almost identical to those present in the X-ray structure. This is an important finding because the ASNS dimer seen by X-ray crystallography contains a disulfide bond that is unlikely to be present in the reducing environment of the cell[37]. We conclude that "head-to-head" dimerization is an intrinsic property of the mammalian enzyme, in contrast to the "head-to-tail" dimerization reported for the bacterial homolog AS-B

(Supplementary Fig. S6)[38]. Second, the EM and X-ray structures both lack density for residues in two loop segments (residues 201-220 and residues 465-475) and the C-terminal tail (residues 539-560 and 536-560 in the EM and X-ray structures, respectively) (Supplementary Fig. S7). Given that the apo-ASNS used to obtain the EM structure was prepared under physiologically relevant conditions, it is likely that these regions are disordered rather than being absent due to proteolysis.

Amino acid side chains pointing into the tunnel (Val-119, Val-141, Arg-142, Leu-255, Met-344, Ala-404 and Leu-415) are also clearly evident in the EM structure (Fig. 2a). These side chains are predominantly hydrophobic, consistent with the idea that ammonia is translocated between the active sites in its neutral form. The presence of a polar side chain close to glutaminase site is therefore interesting, especially because this residue, Arg-142, is conserved in mammalian asparagine synthetases (Supplementary Fig. S8). Ser-362 and Glu-364, which are both located in the part of the tunnel adjacent to the synthetase active site, are also conserved residues (Supplementary Fig. S8). As observed for the X-ray structure of DON-modified human ASNS, the intramolecular tunnel in the EM structure also adopts a "closed", or discontinuous, form through which ammonia cannot diffuse (Fig. 2b and Supplementary Fig. S9a). In contrast, the intramolecular tunnel is continuous when glutamine and AMP are bound within the active sites of the C1A AS-B variant (i.e., it is in an "open" form) (Supplementary Fig. S10)[38]. Given that the covalent modification of Cys-1 does not lead to stabilization of the "open" form of the tunnel, these observations support the idea that AMP binding is critical to permitting ammonia translocation[38,53].

Extracting dynamical motions from the EM map of human ASNS

Competition experiments show that ammonia released from glutamine is not released into solution during asparagine synthesis and must therefore travel along the intramolecular tunnel[43]. This translocation cannot take place when the tunnel is "closed", as seen in the EM and X-ray structures of recombinant human ASNS, suggesting that the gating of the tunnel is

regulated by dynamical motions. To investigate whether these motions are present in the free enzyme or whether they are associated with ligand binding in the synthetase site, we applied 3D variability analysis (3DVA)[54,55] to the EM map of apo-ASNS. As detailed elsewhere[54], local vibrations in the protein structure are preserved by fast-freezing, leading to sample heterogeneity. As a result, 3DVA can identify protein motions from the variance of particle stacks to a volume along a principal component axis (PCA). Analyzing the map of apo-ASNS along five PCAs allowed us to convert the ensemble of EM densities into 100 high-resolution model structures (20 for each PCA), which showed side chain movements in the ammonia tunnel. We were therefore able to understand movements in apo-ASNS at high-resolution (Fig. 3) despite these being smaller than those of larger proteins, such as multidrug ABC exporters[56]. Although no change is seen in two PCAs (components 1 and 3) (Figs. 3b and 3d), the Arg-142 side chain undergoes a drastic conformational change in two PCAs (components 3 and 4) that yields an "open" form of the tunnel (Figs. 3c and 3e). This side chain, however, shows only a slight re-positioning in the fifth PCA (component 5) (Fig. 3f). The simplest interpretation of these results is that interconversion of the "open" and "closed" forms of the tunnel can take place in the absence of bound ligands in the C-terminal synthetase domain, contrary to our initial expectations.

MD simulations of full-length apo-ASNS

We therefore turned to computer-based approaches to validate the conclusions from our 3DVA studies. Various computational methods have been used to study conformational changes and the energetics of ammonia translocation in other glutamine-dependent amidotransferases[57-62]. In order to perform MD simulations, we constructed a model of full-length human ASNS, lacking ligands in both active sites, based on the X-ray coordinates of the DON-modified human enzyme (Supplementary Fig. S11a)[37]. Missing loops and residues 536-560 in the disordered tail were built into the structure using the Robetta server[63]. The resulting model was placed in a box of explicit water molecules and subjected to 200 ns of

simulation at 298.15 K (see Methods). In the initial (t = 0 ns) structure, access to the tunnel from the glutaminase active site is blocked by the side chains of Arg-142 and Leu-415, and this “closed” form persisted for over 80 ns of simulation. By 140 ns into the trajectory, however, the tunnel converted into an ”open” form (Fig. 4a). A detailed analysis of structural snapshots taken throughout the trajectory showed that tunnel opening is a consequence of a 90° reorientation of the Arg-142 side chain, consistent with our EM-based conclusions. The new orientation is stabilized by a salt bridge with the Asp-405 side chain (t = 200 ns); the latter residue is located at the interface between the two domains of the enzyme, providing a molecular basis for the coordination of tunnel opening with domain-domain motions. Forming the Arg-142/Asp-405 interaction requires breaking a network of salt bridges and hydrogen bonds, involving Arg-142, Glu-414, Arg-415 and Asn-75, that is present in the initial (t = 0 ns) structure (Fig. 4c). As the Asn-75 side chain forms the oxyanion hole required for glutamine hydrolysis[65], breaking this network provides a mechanism by which tunnel opening can be coordinated with ammonia release in the glutaminase active site.

In order to assess the extent to which these MD simulations were consistent with experiment, the root mean square fluctuation (RMSF) of backbone heavy atoms for the 100 3DVA-derived EM structures were calculated and compared with RMSF values computed using structures sampled throughout the 200 ns MD simulation[66]. Given the differences in magnitude of the movements determined by MD simulation and those obtained from the restrained coordinates used to construct the EM map, normalized RMSF values were used in the comparison (Fig. 5a). This comparison confirms that the motions revealed by variability analysis correspond to those seen in the MD simulation. Indeed, the small number of residues exhibiting significant differences are those adjacent to missing segments in the EM structure. Equally, the large fluctuations of the C-terminal tail in the MD trajectory are likely a result of these residues being slightly mis-positioned in the initial (t = 0 ns) model. This level of agreement between experiment and theory strongly supports the EM-derived mechanism in which the movement of the Arg-142 side chain regulates tunnel opening and ammonia translocation.

MD simulations of the human ASNS/β-aspartyl-AMP/MgPP$_i$ ternary complex.

We next investigated how ligand binding at the C-terminal synthetase domain might impact the conformational preferences of tunnel residues using a model of the human ASNS/β-aspartyl-AMP/MgPP$_i$ ternary complex (see Methods and Supplementary Fig. S11b). Under identical simulation conditions to those used for apo-ASNS, and despite being in the "closed" form in the initial (t = 0 ns) structure, the tunnel converted to a continuous, open form within 80 ns (Fig. 4b). A detailed analysis of the trajectory for the ternary complex suggests that the presence of β-aspartyl-AMP in the synthetase site leads to salt bridge formation between the Arg-403 side chain and the carboxylate in the intermediate (Supplementary Fig. S12). As a result, Asp-405 can re-position to interact with Arg-142 in its "tunnel open" orientation (Fig. 4c).

DISCUSSION

The successful determination of a cryo-EM structure for human ASNS establishes the physiologically relevant form of the human ASNS dimer and provides a basis for understanding how cytotoxic ASNS inhibitors, which are potential anti-cancer agents[67], might interact with the enzyme[68]. More generally, our findings demonstrate the utility of cryo-EM in providing information on protein motions[69], even at the level of a single residue in an enzyme possessing multiple active sites. The role of Arg-142 in controlling conformational plasticity in the intramolecular tunnel of apo-ASNS contrasts sharply with observations on other Class II amidotransferases in which substrate binding is essential for tunnel formation and activation of glutaminase activity[70]. For example, the presence of 5'-phosphoribosyl-1'-pyrophosphate (PRPP) in the C-terminal active site is required to produce an open form of the intramolecular tunnel in *Escherichia coli* PRPP amidotransferase (Supplementary Fig. S13a)[47]. MD simulations confirm that PRPP binding stabilizes the conformation of a key active site loop, which is disordered in the free enzyme[71]. Large-scale rearrangement of the C-terminal tail in glutamine fructose-6-phosphate amidotransferase (GFAT) is also observed when fructose-6-

phosphate binds to the synthetase site in the C-terminal domain of the enzyme[48], leading to sequestration of the substrate from water and forms part of the ammonia tunnel. The open form of the full-length tunnel linking the synthetase and glutaminase sites in GFAT is only observed, however, when Cys-1 is also covalently modified by DON. Generating the continuous tunnel requires reorientation of the two domains and rotation of the Trp-74 side chain, a structure that is unlikely to be adopted by the free enzyme (Supplementary Fig. S13b)[72]. Our work also suggests that the "open" form of the intramolecular tunnel is energetically favored by the presence of β-aspartyl-AMP in the C-terminal domain of the enzyme. Thus, conformational selection plays a role in the catalytic function of human ASNS[17,18].

Our results suggest that changes in the C-terminal active site are propagated over a distance of approximately 20 Å, leading to tunnel opening and ammonia translocation. Catalytic function in ASNS therefore involves both residues in the active site, which directly interact with substrate and intermediates, and those that define the tunnel connecting the active sites. Hence, conformational selection operates at every step of catalytic turnover in ASNS and is not limited to substrate binding but includes the formation of reactive intermediates. Our results provide an example of how global regulatory mechanisms are embedded within the protein scaffold far away from the active site(s) and emphasize the need to consider the total conformational ensemble of proteins in efforts to obtain enzymes by *de novo* computational design[73].

METHODS

Protein expression and purification.

The expression and purification of wild type human ASNS was carried out as described previously[49], except that 5 mM β-mercaptoethanol was present in all buffers used during

protein purification. Using a spin column, the recombinant enzyme was concentrated to 9 mg/mL in 25 mM Tris-HCl, pH 8.0, containing 250 mM NaCl and 5 mM DTT.

Cryo-EM sample preparation and data collection.

300 mesh UltrAuFoil R1.2/1.3 grids were glow-discharged for 1 minute with a current of 15mA in a PELCO easiGlow system before being mounted onto a Mark IV Vitrobot (FEI/Thermo Fisher Scientific). The sample chamber on the Vitrobot was kept at 4 °C with a relative humidity of 100%. 2.5 µL of the recombinant human ASNS sample at a concentration of 9.0 mg/ml was applied to the grid, which was then blotted from both sides for 4 second with blot force set at 0. After blotting, the grid was rapidly plunge-frozen into a liquid ethane bath cooled by liquid nitrogen.

Single particle data was collected by a 200 kV Glacios transmission electron microscope (FEI/ThermoFisher Scientific) equipped with a Falcon4 camera operated in Electron-Event Representation (EER) mode[74]. Movies were collected using EPU at 150,000x magnification (physical pixel size 0.93 Å) over a defocus range of −0.4 to −2.0 µm and a total accumulated dose of 40 e/ $Å^2$. Camera gain reference was taken at the end of the run. A total of 3,584 movies were acquired. All data processing was carried out in cryoSPARC v3.2.2. Each movie was split into 40 fractions during motion correction with an EER upsampling factor of 1.

Assessing a mode of ASNS dimerization and structure determination.

To gauge how ASNS dimerizes in an unbiased fashion, particles were initially selected using the “blob pick” option in cryoSPARC[51]. 2D class averages showed what appeared to be 2D projections of an ASNS dimer similar to that seen in the X-ray structure[37] (Supplementary Fig. S2b). Further, 769,800 particles were subjected to two rounds of *ab initio* reconstruction, resulting in a total of 12 initial reconstructions (Supplementary Fig. S2d). One reconstruction clearly resembles the head-to-head dimer form of ASNS (compare Supplementary Fig. S2d

and S2e), and the rests exhibited small densities. In light of this observation, particle selection was then carried out by template-based picking, using a template generated from the X-ray structure (PDB: 6GQ3) in UCSF Chimera[75]. The full cryo-EM data processing workflow is illustrated in Supplementary Fig S3. Bad particles were removed using several rounds of 2D classification followed by 5 rounds of *ab initio* reconstructions, and successive heterologous refinement, non-uniform refinement with CTF and defocus correction, and the imposition of C_2 symmetry gave rise to a map with 3.5 Å overall resolution. The map was sharpened using the program DeepEMhancer[76] as implemented on the COSMIC[2] site[77]. Model building started with fitting the crystal structure (PDB: 6GQ3)[37] into the EM map using rigid body refinement by REFMAC[78]. The resulting model was then iteratively refined by real-space refinement in Phenix[79] followed by manual inspection and refinement in Coot[80]. Figures for the cryo-EM density maps and models were generated with Chimera[75] or ChimeraX[81].

3D variability analysis (3DVA) of the EM map for human ASNS.

The EM map was subjected to 3D variability analysis (3DVA) in cryoSPARC v3.2.2 with 5 principal components at 4 Å resolution with the mask previously used in a final non-uniform refinement[51]. A movie for each component was made with UCSF Chimera[75] using frames generated by the 3DVA display program in a simple mode in cryoSPARC v3.2.2 (Supplementary Movies M1-M5). Movie frames were subjected to variability refinement in Phenix, using 50 models per map, and a resolution of 4 Å, yielding a series of 20 models per component. Backbone RMS fluctuations for each residue in the set of 100 structures were computed using the CPPTRAJ software package[66].

Molecular dynamics simulations.

The Robetta server[63] was used to build a model of **full-length** human ASNS by adding residues to the X-ray structure that are not observed in the electron density map. In addition, the unmodified side chain of Cys-1 was restored by deleting atoms in the DON ligand and

adding hydrogen atoms. The chloride anion bound between the N- and C-terminal domains in the X-ray structure was retained in the apo-ASNS model. The ternary complex was obtained by positioning the Mg(II) salt of inorganic pyrophosphate (PP_i) into this apo-ASNS model such that it was in an identical location to that observed in GMP synthetase[82] and other members of the PP-loop ATP pyrophosphatase superfamily[83]. β-aspartyl-AMP was docked into the model of the binary complex so that the nucleobase was in a similar site to that seen for AMP in the X-ray crystal structure of the bacterial enzyme[38]. The hydrogen bonding networks in each of the models were then optimized, and the protonation state of ionizable residues at pH 7.4 determined by calculation. As a result, the amino and carboxylate groups of the aspartate-derived portion of β-aspartyl-AMP formed complementary electrostatic and hydrogen bonding interactions with Gly-365, Asp-367, Glu-368 and Arg-403 (Supplementary Fig. S11). These four residues are conserved in known glutamine-dependent asparagine synthetases (Supplementary Fig. S8).

Each of these models was energy minimized before being placed in a box of TIP3P water molecules[84], which was sized to ensure a minimum distance of 10 Å between protein atoms and the sides of the box. After the addition of sodium ions to neutralize the total charge of the system, each model was heated to 300 K and equilibrated in the NPT ensemble. Each of the models was then subject to NPT MD simulations of 200 ns using the OPLS_2005 force field[85] to describe the protein and ligands. These calculations were performed using the DESMOND package (D.E. Shaw Research, New York, NY, 2018). Snapshots were taken at 200 ps intervals in both simulations (Supplementary Movies M6 and M7) and analyzed using CAVER 3.0 to identify intramolecular tunnels in the sampled protein structures[64]. Backbone RMS fluctuations for structures in the two MD trajectories were computed using CPPTRAJ[66].

Data Availability

Structural data have been deposited in the PDB (PDB ID: 8SUE) and the Electron Microscopy Data Bank (EMDB ID: EMD-40764). Coordinate files for the 100 structures used in the 3DVA study and/or the two MD-derived trajectories are available on request.

FIGURE LEGENDS

Fig. 1. | Cryo-EM structure of human ASNS. **a** Schematic representation showing the N-terminal glutaminase (forest green), dimerization (magenta) and the C-terminal synthetase (cornflower blue) domains. The glutamine-binding (orange red) and synthetase active site (orange) are also indicated together with residues constituting the intramolecular tunnel (red). **b** EM map and **c** ribbon representation of human ASNS (coloring is identical to that used in **a**). **d** Close-up view of the dimerization motif showing the salt bridges (left) and hydrophobic cluster (right).

Fig. 2. | **a** Superimposition of residues defining the intramolecular tunnel in the EM (colored as in Fig. 1a) and X-ray (white) structures of human ASNS. **b** Internal cavity and pocket representations, as computed by PyMol, showing the discontinuous tunnels in the EM (left) and X-ray (right) structures. The N- and C-terminal domains of both structures are colored green and blue, respectively, with colored circles showing the two active sites. Dashed lines connecting the active sites represent the position of the open tunnel seen in the X-ray crystal structure of the bacterial enzyme (Supplementary Fig. S11).

Fig. 3. | PCA-derived structures of the ammonia tunnel in human ASNS obtained from 3D variability analysis. **a** Side view of critical residues (Val-141, Arg-142, Glu-364, Val-401, Ala-404, Val-414, Leu-415) constituting the ammonia tunnel derived from the consensus EM map. The side chain of Arg-142 that blocks the tunnel is indicated (red circle). Side view of critical residues constituting ammonia tunnel derived from the variable EM maps derived from 3DVA. Critical residues constituting ammonia tunnel derived from variable maps at frame 1 (one end) and frame 20 (the other end) are superimposed: **b** PCA component 1, **c** PCA component 2, **d** PCA component 3, **e** PCA component 4, **f** PCA component 5.

Fig. 4. | Snapshots from the MD trajectories computed for **a** human ASNS and **b** the human ASNS/β-aspartyl-AMP/$MgPP_i$ ternary complex. Tunnels were identified using the CAVER 3.0 software package[64]. **c** Superimposed snapshots from the MD trajectory of the human ASNS/β-aspartyl-AMP/$MgPP_i$ ternary complex showing the reorientation of the Arg-142 side chain (t = 0 ns, blue; t = 200 ns, green).

Fig. 5. | Normalized RMSF values for residues in human ASNS. **a** Comparison of values from the 100 3DVA-derived structures of chain A (blue) and the MD trajectory of apo-ASNS (red). **b** Comparison of values from the MD trajectories of apo-ASNS (red) and the human ASNS/β-aspartyl-AMP/$MgPP_i$ ternary complex (teal).

REFERENCES

1. Schwartz, S. D. Protein dynamics and enzymatic catalysis. *J. Phys. Chem. B* **127**, 2649-2660 (2023)
2. Klinman, J. P. Dynamical activation of function in metalloenzymes. *FEBS Lett.* **597**, 79-91 (2023).
3. Xu, D., Meisburger, S. & Ando, N. Correlated motions in structural biology. *Biochemistry* **60**, 2331-2340 (2021).
4. Agarwal, P. K. A biophysical perspective on enzyme catalysis. *Biochemistry* **58**, 438-449 (2019).
5. Nashine, V. C., Hammes-Schiffer, S. & Benkovic, S. J. Coupled motions in enzyme catalysis. *Curr. Op. Chem. Biol*. **14**, 644-651 (2010).
6. Warshel, A. & Bora, R. P. Defining and quantifying the role of dynamics in enzyme catalysis. *J. Chem. Phys.* **144**, 180901 (2016).
7. Klinman, J. P., Offenbacher, A. R. & Hu, S. Origins of enzyme catalysis: Experimental findings for C-H activation, new models, and their relevance to prevailing theoretical constructs. *J. Am. Chem. Soc*. **139**, 18409-18427 (2017).
8. Guo, J. & Zhou, H.-X. Protein allostery and conformational dynamics. *Chem. Rev.* **116**, 6503-6515 (2016).
9. Offenbacher, A. R., Iavarone, A. T. & Klinman, J. P. Hydrogen-deuterium exchange reveals long-range dynamical allostery in soybean lipoxygenase. *J. Biol. Chem.* **293**, 1138-1148 (2018).
10. Bunzel, H. A., Anderson, J. L. R., Hilvert, D., Arcus, V. L., van der Kamp, M. W. & Mulholland, A. J. Evolution of dynamical networks enhances catalysis in a designer enzyme. *Nat. Chem.* **13**, 1017-1022 (2021).
11. Otten, R., Pádua, R. A. P., Bunzel, H. A., Nguyen, V., Pitsawong, W., Patterson, M., Sui, S., Perry, S. L., Cohen, A. E., Hilvert, D. & Kern, D. How directed evolution reshapes the energy landscape in an enzyme to boost catalysis. *Science* **370**, 1442-1446 (2020).

12. Joo, H., Lin, Z. & Arnold, F. H. Laboratory evolution of peroxide-mediated cytochrome P450 hydroxylation. *Nature* **399**, 670-673 (1999).
13. Wang, Y., Xue, P., Cao, M., Yu, T., Lane, S. T. & Zhou, H. Directed evolution: Methodologies and applications. *Chem. Rev.* **121**, 12384-12444 (2021).
14. Zaragoza, J. P. T., Offenbacher, A. R., Hu, S., Gee, C. L., Firestein, Z. M., Minnetian, N., Deng, Z., Fan, F., Iavarone, A. T. & Klinman, J. P. Temporal and spatial resolution of distal protein motions that activate hydrogen tunneling in soybean lipoxygenase. *Proc. Acad. Natl. Sci., USA* **120**, e2211630120 (2023).
15. Gao, S, & Klinman, J. P. Functional roles of enzyme dynamics in accelerating active site chemistry: Emerging techniques and changing concepts. *Curr. Op. Struct. Biol.* **75**, 102434 (2022).
16. Åqvist, J., Socan, J. & Purg, M. Hidden conformational states and strange temperature optima in enzyme catalysis. *Biochemistry* **59**, 3844-3855 (2022).
17. Henzler-Wildman, K. A., Lei, M., Thai, V., Kerns, S. J., Karplus, M. & Kern, D. A hierarchy of timescales in protein dynamics is linked to enzyme catalysis. *Nature* **450**, 913-917 (2007).
18. Eisenmesser, E. Z., Millet, O., Labeikovsky, W., Korzhnev, D. M., Wolf-Watz, M., Bosco, D. A., Skalicky, J. J., Kay, L. E. & Kern, D. Intrinsic dynamics of an enzyme underlies catalysis. *Nature* **438**, 117-121 (2005).
19. Zalkin, H. & Smith, J. L. Enzymes using glutamine as a nitrogen donor. *Adv. Enzymol. Relat. Areas Mol. Biol.* **72**, 87-144 (1998).
20. Huang, X., Holden, H. M. & Raushel, F. M. Channeling of substrates and intermediates in enzyme-catalyzed reactions. *Annu. Rev. Biochem.* **70**, 149-180 (2001).
21. Richards, N. G. J. et al. in *Comprehensive Natural Products II: Chemistry & Biology* Vol. 8 Ch. 6 (Elsevier, 2010).
22. Pan, P., Woehl, E. & Dunn, M. F. Protein architecture, dynamics and allostery in tryptophan synthase. *Trends Biochem. Sci.* **22**, 22-27 (1997).

23. Kovermann, M., Rogne, P. & Wolf-Watz, M. Protein dynamics and function from solution state NMR spectroscopy. *Q. Rev. Biophys.* **49**, e6 (2016).
24. Meisburger, S., Case, D. A. & Ando, N. Robust total X-ray scattering workflow to study correlated motions of proteins in crystals. *Nat. Commun.* **14**, 1228 (2023).
25. Thompson, M. C. et al. Temperature-jump solution X-ray scattering reveals distinct motions in a dynamic enzyme. *Nat. Chem.* **11**, 1058-1066 (2019).
26. Orville, A. M. Recent results in time resolved serial femtosecond crystallography at XFELs. *Curr. Op. Struct. Biol.* **65**, 193-208 (2020).
27. Beton, J. G., Cragnolini, T., Kaleel, M., Mulvaney, T., Sweeney, A. & Topf, M. Integrating model simulation tools and cryo-electron microscopy. *WIREs Comput. Mol. Sci.* e1642 (2023).
28. Vant, J. W., Sarkar, D., Nguyen, J., Baker, A. T., Vermaas, J. V. & Singharoy, A. Exploring cryo-electron microscopy with molecular dynamics. *Biochem. Soc. Trans.* **50**, 569-581 (2022).
29. Matsumoto, S., Ishida, S., Araki, M., Terayama, K. & Okuno, Y. Extraction of protein dynamics information from cryo-EM maps using deep learning. *Nat. Mach. Intel.* **3**, 153-160 (2021).
30. Tsai, M.-D., Wu, W.-J. & Ho, M.-C. Enzymology and dynamics by cryogenic electron microscopy. *Annu. Rev. Biophys.* **15**, 19-38 (2022)
31. Richards, N. G. J. & Schuster, S. M. Mechanistic issues in asparagine synthetase catalysis. Adv. Enzymol. *Relat. Areas Mol. Biol.* **72**, 145-198 (1998).
32. Lomelino, C., Andring, J. T., McKenna, R. & Kilberg, M. S. Asparagine synthetase: Function, structure, and role in disease. *J. Biol. Chem.* **292** 19952-19958 (2017).
33. Knott, S. R. V. et al. Asparagine bioavailability governs metastasis in a model of breast cancer. *Nature* **554**, 378-381 (2018).
34. Hettmer, S. et al. Functional genomic screening reveals asparagine dependence as a metabolic vulnerability in sarcoma. *eLife* **4**, e09436 (2015).

35. Jedraszek, K., Malczewska, M., Parysek-Wojcik, K. & Lejman, M. Resistance mechanisms in pediatric B-call acute lymphoblastic leukemia. *Int. J. Mol. Sci.* **23**, 3067 (2022).
36. Staklinski, S. J. et al. Cellular and molecular characterization of two novel asparagine synthetase gene mutations linked to asparagine synthetase deficiency. *J. Biol. Chem.* **298**, 102385 (2022).
37. Zhu, W. et al. High-resolution crystal structure of human asparagine synthetase enables analysis of inhibitor binding and selectivity. *Commun. Biol.* **2**, 345 (2019).
38. Larsen, T. M. et al. Three-dimensional structure of *Escherichia coli* asparagine synthetase B: A short journey from substrate to product. *Biochemistry* **38**, 16146-16157 (1999).
39. Boehlein, S. K., Richards, N. G. J. & Schuster, S. M. Glutamine-dependent nitrogen transfer in Escherichia coli asparagine synthetase B. *J. Biol. Chem.* **269**, 7450-7457 (1994).
40. Boehlein, S. K., Stewart, J. D., Walworth, E. S., Thirumoorthy, R., Richards, N. G. J. & Schuster, S. M. Kinetic mechanism of *Escherichia coli* asparagine synthetase B. *Biochemistry* **37**, 13230-13237 (1998).
41. Pfeiffer, N. E., Mehlhaff, P. M., Wylie, D. E. & Schuster, S. M. Topographical separation of the catalytic sites of asparagine synthetase explored with monoclonal antibodies. *J. Biol. Chem.* **262**, 11565-11570 (1987).
42. Richards, N. G. J., Humkey, R. N., Li, K., Meyer, M. E. & Sintjago de Cordova, T. C., in *Comprehensive Natural Products II: Chemistry & Biology* Vol. 8 Ch. 6 (Elsevier, 2010).
43. Li, K. K., Beeson, W. T., Ghiviriga, I. & Richards, N. G. J. A convenient gHMQC-based NMR assay for investigating ammonia channeling in glutamine-dependent amidotransferases: Studies of *Escherichia coli* asparagine synthetase. *Biochemistry* **46**, 4840-4849 (2007).
44. Wu, M. & Lander, G. C. Present and emerging methodologies in cryo-EM single-particle analysis. *Biophys. J.* **119**, 1281-1289 (2020).

45. Petrovic, D. & Kamerlin, S. C. L. Molecular modelling of conformational dynamics and its role in enzyme evolution. *Curr. Op. Struct. Biol.* **52**, 50-57 (2018).

46. Norberg, J. & Nilsson, L. Advances in biomolecular simulations: methodology and recent applications. *Q. Rev. Biophys.* **36**, 257-306 (2003).

47. Krahn, J. M., Kim, J. H., Burns, M. R., Parry, R. J., Zalkin, H. & Smith, J. L. Coupled formation of an amidotransferase ammonia tunnel and a phosphoribosyltransferase active site. *Biochemistry* **36**, 11061-11068 (1997).

48. Mouilleron, S., Badet-Denisot, M.-A. & Golinelli-Pimpaneau, B. Ordering of C-terminal loop and glutaminase domains of glucosamine-6-phosphate synthase promotes sugar ring opening and formation of the ammonia channel. *J. Mol. Biol.* **377**, 1174-1185 (2008).

49. Ciustea, M., Gutierrez, J. A., Abbatiello, S. E., Eyler, J. R. & Richards, N. G. J. Efficient expression, purification and characterization of C-terminally tagged, recombinant human asparagine synthetase. *Arch. Biochem. Biophys.* **440**, 18-27 (2005).

50. Imasaki, T., Wenzel, S., Yamada, K., Bryant, M. L. & Takagi, Y. Titer estimation for quality control (TEQC) method: A practical approach for optimal production of protein complexes using the baculovirus expression vector system. *PloS ONE* **13**, e0195356 (2018).

51. Punjani, A., Rubinstein, J. L., Fleet, D. J. & Brubaker, M. A. cryoSPARC: Algorithms for rapid unsupervised cryo-EM structure determination. *Nat. Methods* **14**, 290-296 (2017).

52. Jayaram, H. N., Cooney, D. A., Milman, H. A., Homan, E. R. & Rosenbluth, R. J. DON, CONV and DONV I. Inhibition of L-asparagine synthetase *in vitro*. *Biochem. Pharmacol.* **25**, 1571-1582 (1976).

53. Tesson, A. R., Soper, T. S., Ciustea, M. & Richards, N. G. J. Revisiting the steady state kinetic mechanism of glutamine-dependent asparagine synthetase from *Escherichia coli*. *Arch. Biochem. Biophys.* **413**, 23-31 (2003).

54. Afonine, P. V., Gobet, A., Moissonnier, L., Martin, J., Poon, B. K. & Chaptal, V. Conformational space exploration of cryo-EM structures by variability refinement. *Biochim. Biophys. Acta Biomembranes* **1865**, 184133 (2023).

55. Punjani, A. & Fleet, D. J. 3D variability analysis: Resolving continuous flexibility and discrete heterogeneity from single particle cryo-EM. *J. Struct. Biol.* **213**, 107702 (2021).
56. Chaptal, V. et al. Substrate-bound and substrate-free outward-facing structures of a multidrug ABC exporter. *Sci. Adv.* **8**, eabg9215 (2022).
57. Sharma, N., Singh, S., Tanwar, A. S., Mondal, J. & Anand, R. Mechanism of coordinated gating and signal transduction in purine biosynthetic enzyme formylglycinamidine synthetase. *ACS Catalysis* **12**, 1930-1944 (2022).
58. Fan, Y., Lund, L., Yang, L., Raushel, F. M. & Gao, Y.-Q. Mechanism for transport of ammonia within carbamoyl phosphate synthetase determined by molecular dynamics simulations. *Biochemistry* **47**, 2935-2944 (2008).
59. Fan, Y., Lund, L., Shao, Q., Gao, Y.-Q. & Raushel, F. M. A combined theoretical and experimental study of the ammonia tunnel in carbamoyl phosphate synthetase. *J. Am. Chem. Soc.* **131**, 10211-10219 (2009).
60. Dewage, S. W. & Cisneros, G. A. Computational analysis of ammonia transfer along two intramolecular tunnels in *Staphylococcus aureus* glutamine-dependent amidotransferase (GatCAB). *J. Phys. Chem. B* **119**, 3669-3677 (2015).
61. Amaro, R., Myers, R. S., Davisson, V. J. & Luthey-Schulten, Z. A. Structural elements in IGP synthase exclude water to optimize ammonia transfer. *Biophys. J.* **89**, 475-487 (2005).
62. Wang, X. S., Roitberg, A. E. & Richards, N. G. J. Computational studies of ammonia channel function in glutamine 5'-phosphoribosylpyrophosphate amidotransferase. *Biochemistry* **48**, 12272-12282 (2009).
63. Kim, D. E., Chivian, D. & Baker, D. Protein structure prediction and analysis using the Robetta server. *Nucl. Acids Res.* **32**, W526-W531 (2004).
64. Chovancova, E. et al. CAVER 3.0: A tool for the analysis of transport pathways in dynamic protein structures. *PloS Comput. Biol.* **8**, e1002708 (2012).

65. Boehlein, S. K., Rosa-Rodriguez, J. G., Schuster, S. M. & Richards, N. G. J. Catalytic activity of the N-terminal domain of *Escherichia coli* asparagine synthetase B can be reengineered by single-point mutation. *J. Am. Chem. Soc.* **119**, 5785-5791 (1997).
66. Roe, D. R. & Cheatham, T. E., III PTRAJ and CPPTRAJ: Software for processing and analysis of molecular dynamics trajectory data. *J. Chem. Theory Comput.* **9**, 3084-2095 (2013).
67. Chiu, M., Taurino, G., Bianchi, M. G., Kilberg, M. S. & Bussolati, O. Asparagine synthetase in cancer: Beyond acute lymphoblastic leukemia. *Front. Oncol.* **9**, 1480 (2020).
68. Ikeuchi, H. et al. A human asparagine synthetase inhibitor kills asparaginase-resistant MOLT-4 cells. *Bioorg. Med. Chem.* **20**, 5915-5927 (2012).
69. Zhong, E. D., Bepler, T., Berger, B. & Davis, J. H. CryoDRGN: Reconstructions of heterogeneous cryo-EM structures using neural networks. *Nat. Methods* **18**, 176-185 (2021).
70. Mouilleron, S. & Golinelli-Pimpaneau, B. Conformational changes in ammonia-channeling glutamine amidotransferases. *Curr. Op. Struct. Biol.* **17**, 653-664 (2007).
71. Li, C. et al. Conformational changes of glutamine 5'-phosphoribosylpyrophosphate amidotransferase for two substrate analogue binding: Insight from conventional molecular dynamics and accelerated molecular dynamics simulation. *Front. Chem.* **9**, 640994 (2021).
72. Mouilleron, S., Badet-Denisot, M.-A. & Golinelli-Pimpaneau, B. Glutamine binding opens the ammonia channel and activates glucosamine-6P synthase. *J. Biol. Chem.* **281**, 4404-4412 (2006).
73. Welborn, V. V. & Head-Gordon, T. Computational design of synthetic enzymes. *Chem. Rev.* **119**, 6613-6630 (2019).
74. Guo, H. et al. Electron-event representation data enable efficient cryoEM file storage with full preservation of spatial and temporal resolution. *IUCr J.* **7**, 860-869 (2020).
75. Pettersen, E. et al. UCSF Chimera – A visualization system for exploratory research and analysis. *J. Comput. Chem.* **25**, 1605-1612 (2004).

76. Sanchez-Garcia, R. et al. DeepEMhancer: A deep learning solution for cryo-EM volume post-processing. *Commun Biol* **4**, 874 (2021).

77. Cianfrocco, M. A., Wong-Barnum, M., Youn, C., Wagner, R. & Leschziner, A. in *Proceedings of the Practice and Experience in Advanced Research Computing 2017 on Sustainability, Success and Impact* (Association for Computing Machinery, 2017).

78. Murshudov, G. N., Vagin, A. A. & Dodson, E. J. Refinement of macromolecular structures by the maximum-likelihood method. *Acta Crystallogr. D Biol. Crystallogr.* **53**, 240-255 (1997).

79. Adams, P. et al. PHENIX: A comprehensive Python-based system for macromolecular structure solution. *Acta Crystallogr. D Biol. Crystallogr.* **66**, 213-221 (2010).

80. Emsley, P., Lohkamp, B., Scott, W. G. & Cowtan, K. Features and development of Coot. *Acta Crystallogr. D Biol. Crystallogr.* **66**, 486-501 (2010).

81. Pettersen, E. et al. UCSF ChimeraX: Structure visualization system for researchers, educators, and developers. *Protein Sci.* **30**, 70-82 (2021).

82. Tesmer, J. J. G., Klem, T. J., Deras, M. L., Davisson, V. J. & Smith, J. L. The crystal structure of GMP synthetase reveals a novel catalytic triad and is a structural paradigm for two enzyme families. *Nat. Struct. Biol.* **3**, 74-86 (1996).

83. Fellner, M., Hausinger, R. P. & Hu, J. A structural perspective on the PP-loop ATP pyrophosphatase family. *Crit. Rev. Biochem. Mol. Biol.* **53**, 607-622 (2018).

84. Jorgensen, W. L., Chandrasekhar, J., Madura, J., Impey, R. W. & Klein, M. L. Comparison of simple potential functions for simulating liquid water. *J. Chem. Phys.* **79**, 926-935 (1983).

85. Kaminski, G. A., Friesner, R. A., Tirado-Rives, J. & Jorgensen, W. L. Evaluation and reparametrization of the OPLS-AA force field for proteins via comparison with accurate quantum chemical calculations on peptides. *J. Phys. Chem. B* **105**, 6474-6487 (2001).

Acknowledgements

The authors would like to acknowledge Indiana University School of Medicine EM facility and NIH/NIGMS, S10 OD028723 for supporting this work. Additional funds for the EM structure determination were provided by the Indiana University School of Medicine (Y. T.), and, in part, NIGMS award number R01GM111695 (Y. T.). This work was also supported by the CNRS (V. C.), and the French National Research Agency grant number ANR-19-CE11-0023-01 (V. C.). Funding for the computational studies was provided by the Biotechnology and Biological Sciences Research Council, grant number P/0118017/1 (N. G. J. R.), by the European Committee grant number FESR FSE 2014- 2020 (S. A.), and by Regione Calabria (S. A). C.G. was supported by funds from the EU, project number FSE-FESR PON-RI 2014-2020. The content is solely the responsibility of the authors and does not necessarily represent the official views of the Indiana University School of Medicine. The European Committee and Regione Calabria also decline any responsibility concerning the use of the information disclosed in the paper.

Author Contributions

A.C., W.Z., Y.T., S.A. and N.G.J.R. designed the research. Y.T. and M.V. collected data, and Y.T. solved the EM structure. V.C. and Y.T. carried out the 3D variability analysis. A.C., A.L. and C.G. performed the computer simulations under the guidance of S.A. The MD simulation data were analyzed by A.C., C.G., W.Z. and N.G.J.R. Finally, the paper was co-written by W.Z., Y.T. and N.G.J.R. with input from all other authors.

Competing Interests

The authors declare no competing interests. The funders had no role in the design of the study; in the collection, analyses, or interpretation of data; in the writing of the manuscript, or in the decision to publish the results.

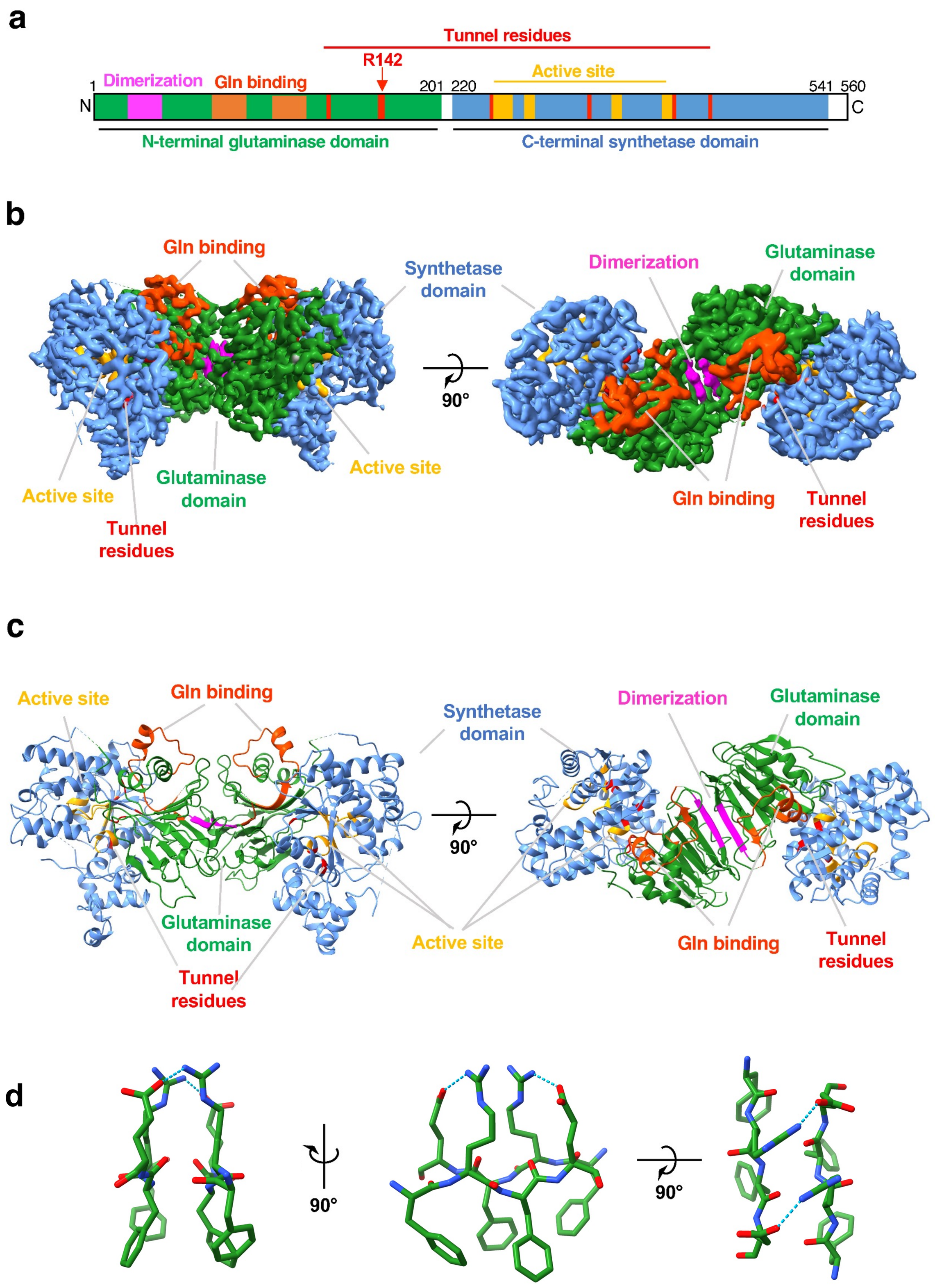
a
Tunnel residues
R142
Active site
1
Dimerization
Gln binding
201
220
541
560
N
C
N-terminal glutaminase domain
C-terminal synthetase domain
b
Gln binding
Synthetase domain
Dimerization
Glutaminase domain
90°
Active site
Glutaminase domain
Active site
Tunnel residues
Gln binding
Tunnel residues
c
Active site
Gln binding
Synthetase domain
Dimerization
Glutaminase domain
90°
Glutaminase domain
Active site
Gln binding
Tunnel residues
Tunnel residues
d
90°
90°

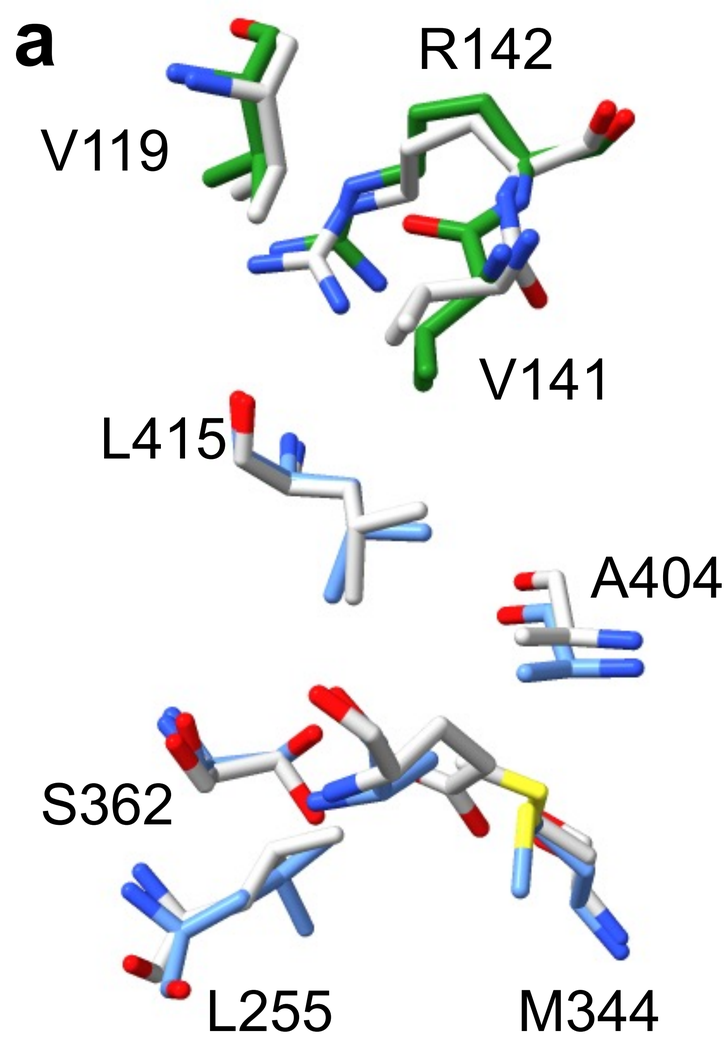
a
R142
V119
V141
L415
A404
S362
L255
M344

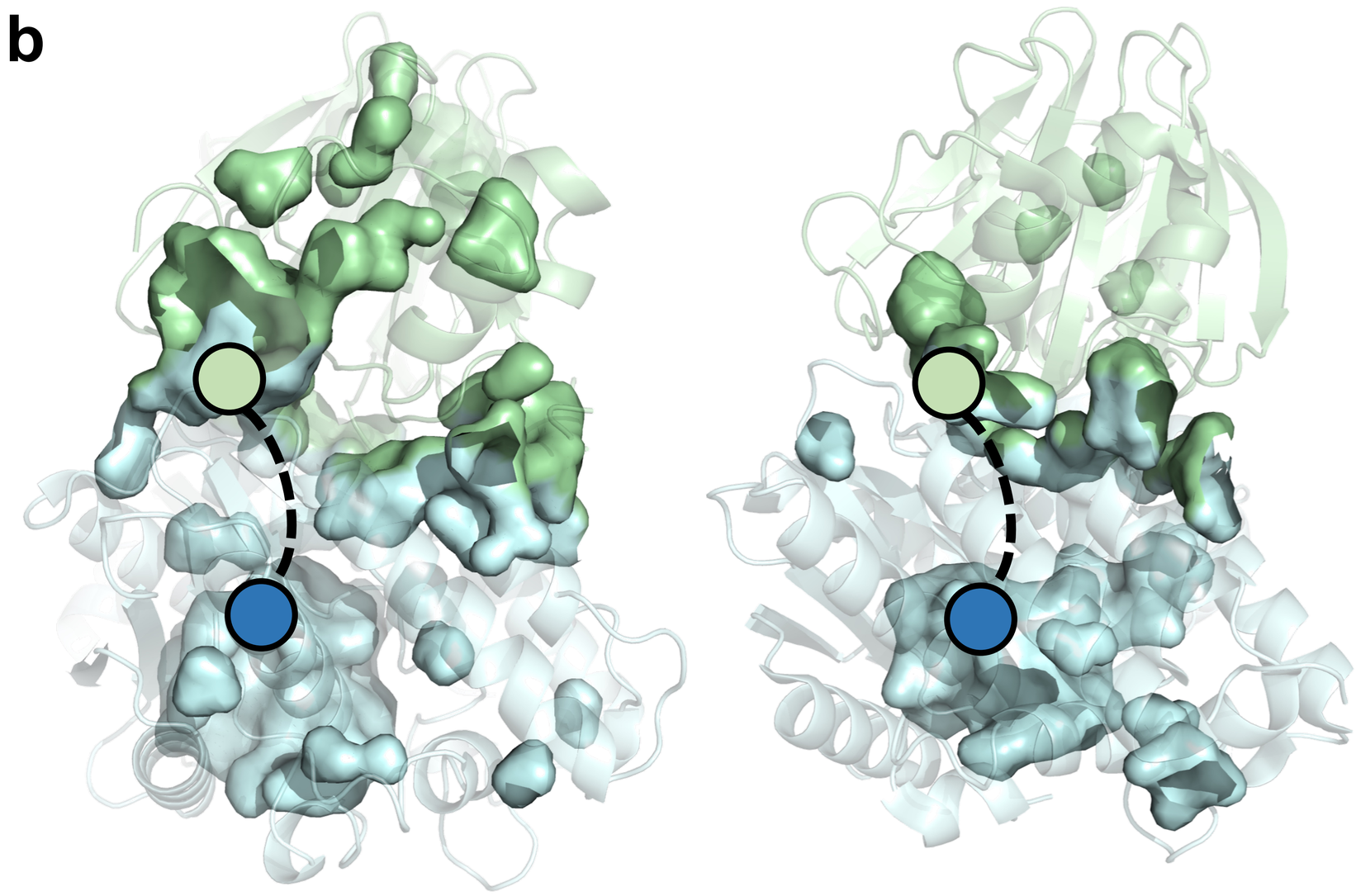
b

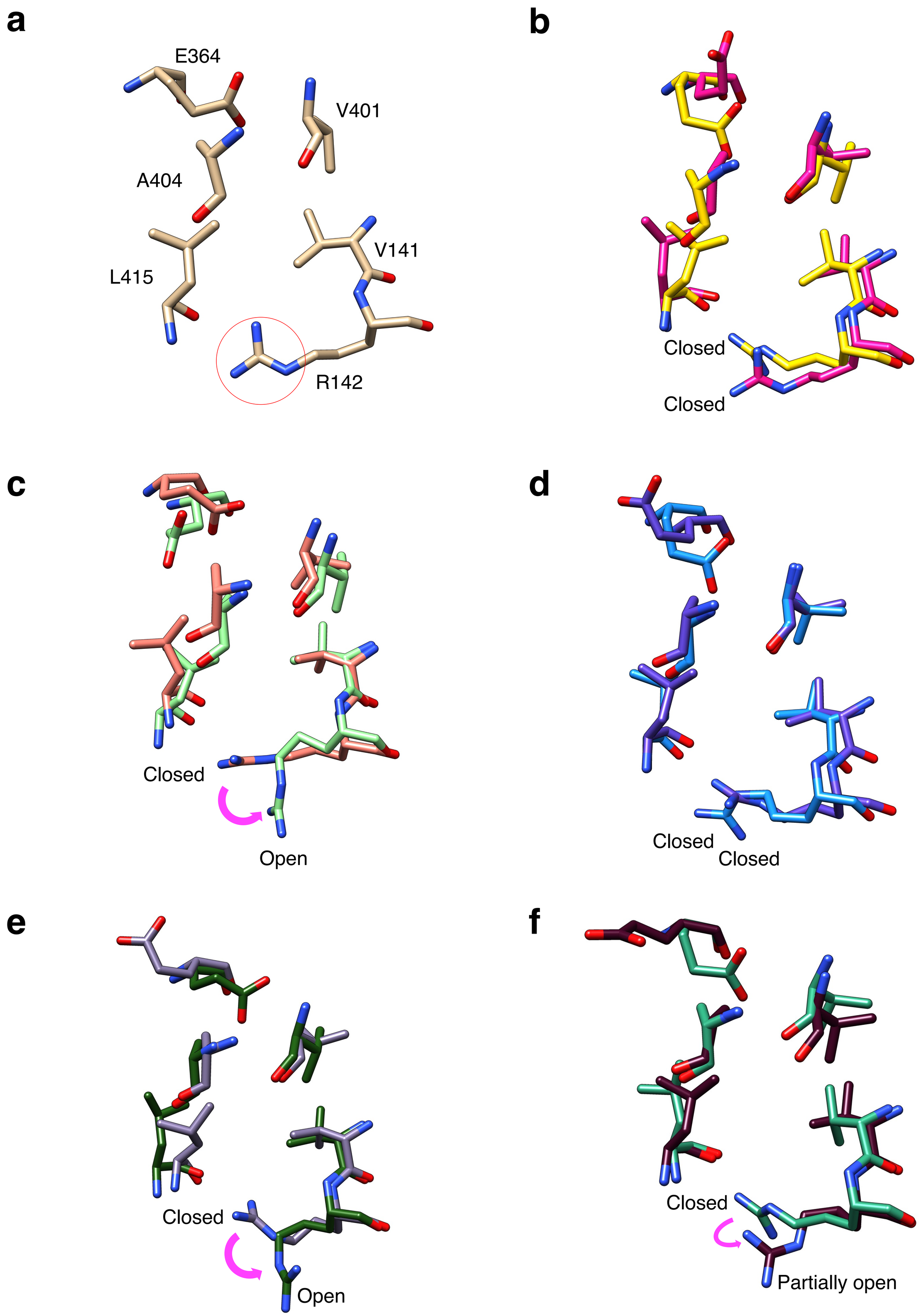
a
E364
V401
A404
V141
L415
R142
b
Closed
Closed
c
Closed
Open
d
Closed
Closed
e
Closed
Open
f
Closed
Partially open

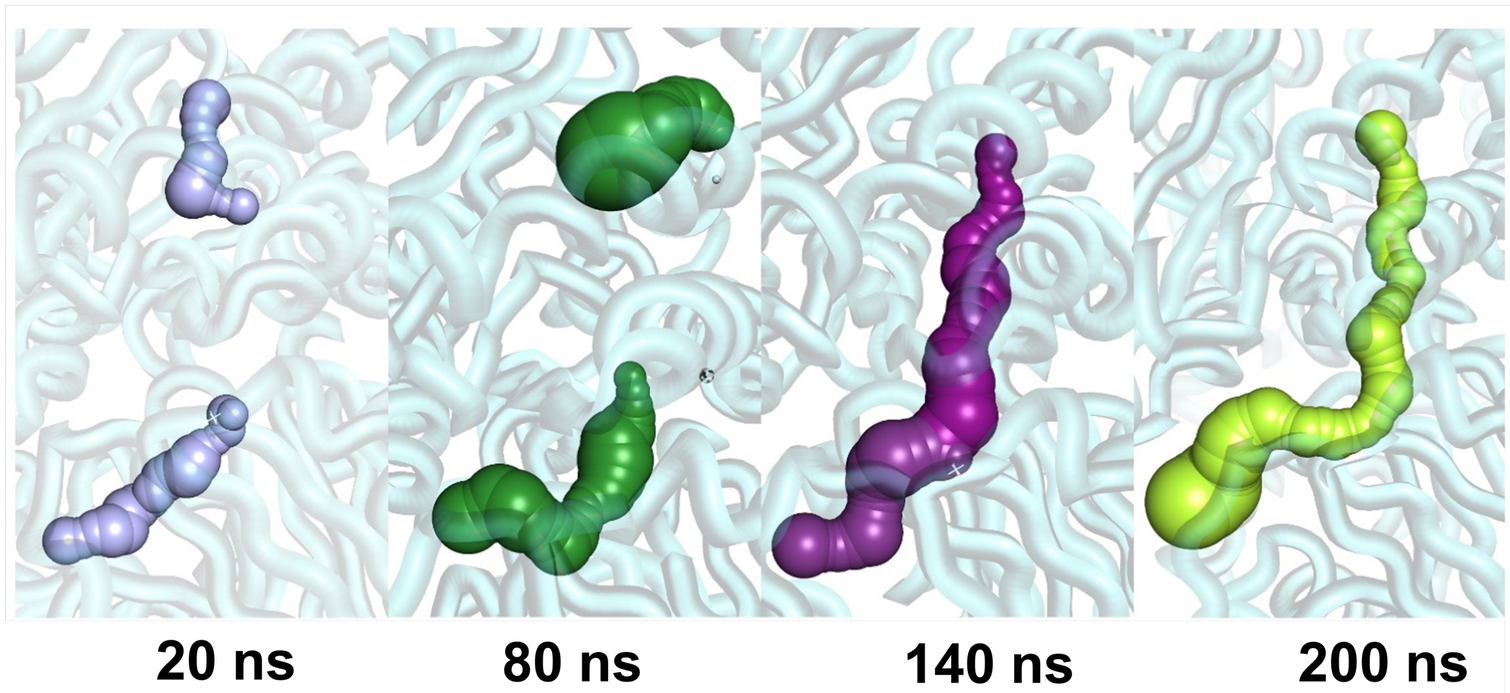
a
20 ns
80 ns
140 ns
200 ns

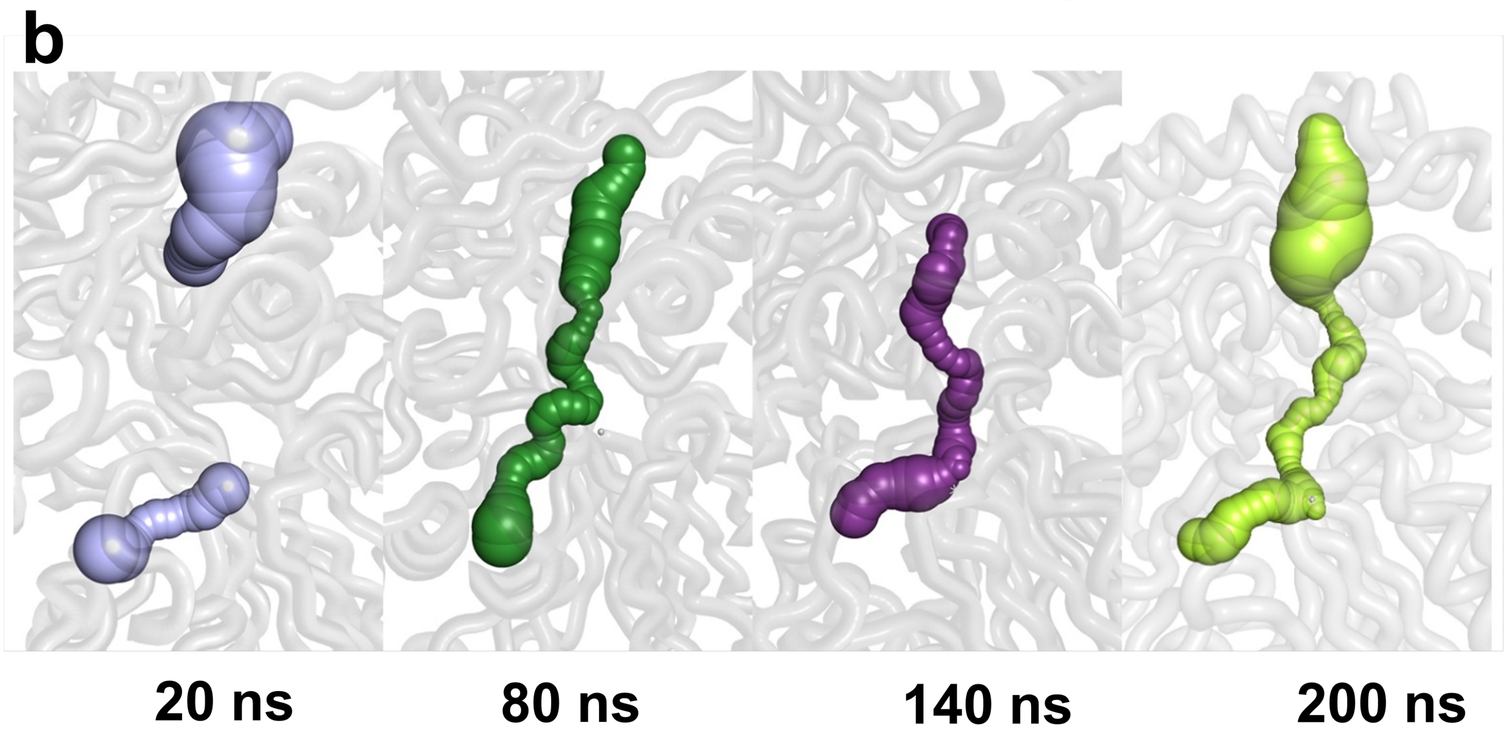
b
20 ns
80 ns
140 ns
200 ns

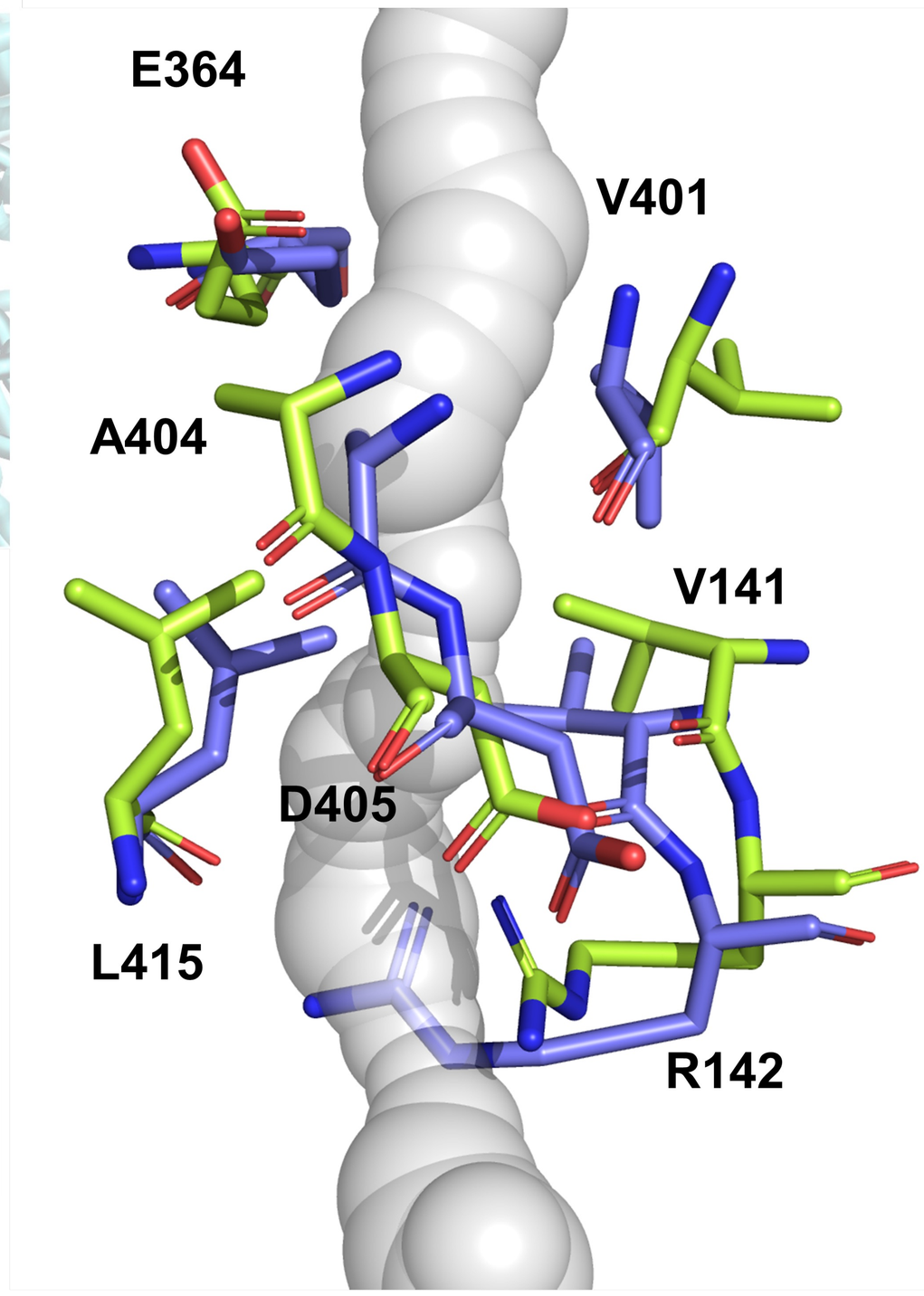
c
E364
V401
A404
V141
D405
L415
R142

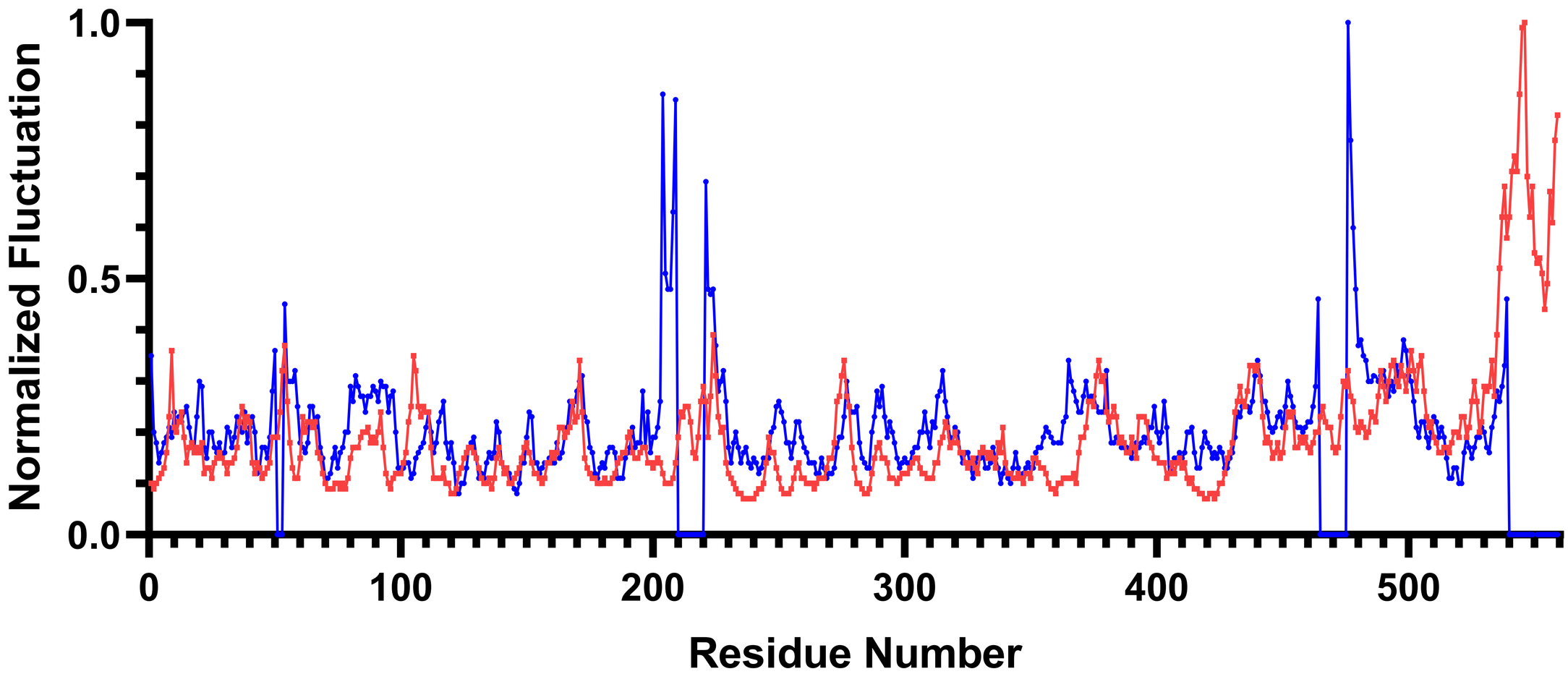
a
Normalized Fluctuation
1.0
0.5
0.0
0
100
200
300
400
500
Residue Number

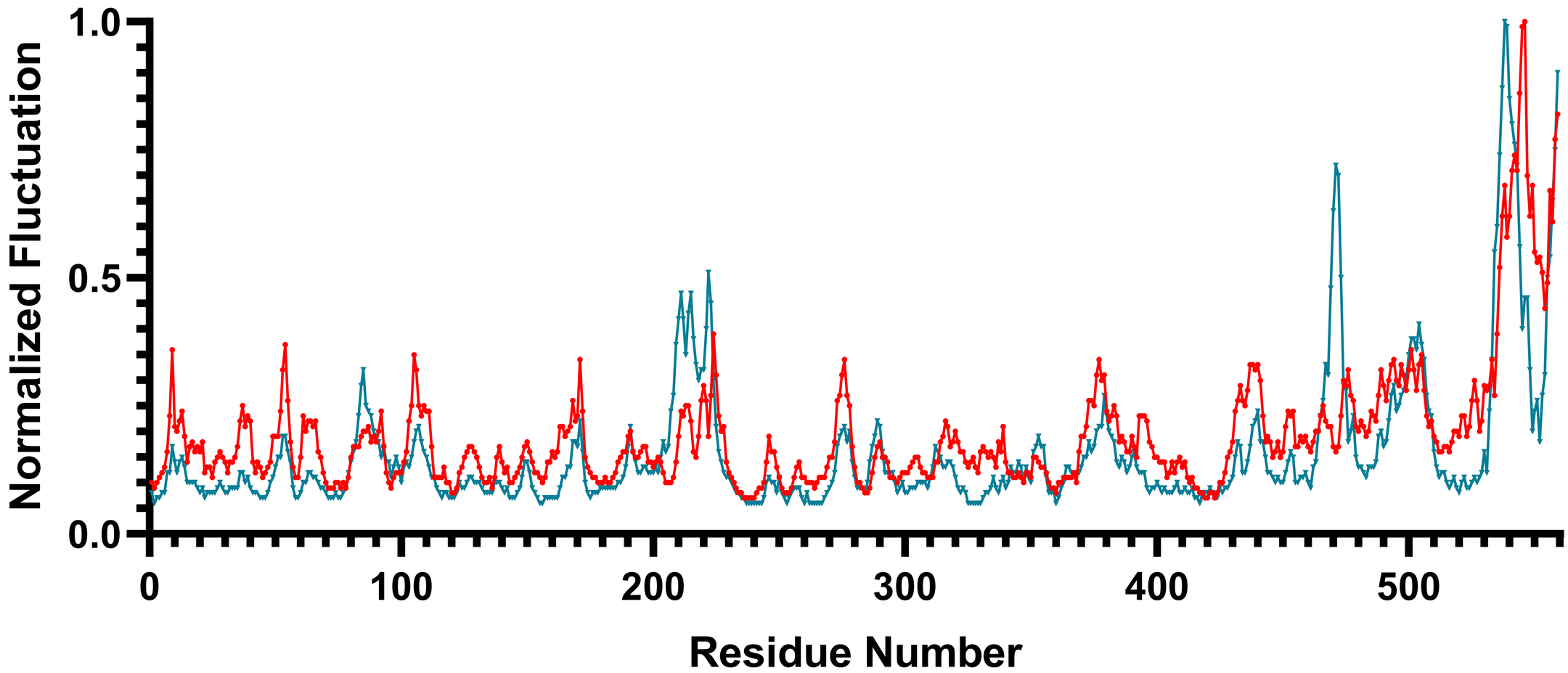
b
Normalized Fluctuation
1.0
0.5
0.0
0
100
200
300
400
500
Residue Number